SCIENCE CHINA
Chemistry

•ARTICLES•

https://doi.org/10.1007/s11426-019-9590-6

Active sites in CO_2 hydrogenation over confined VO_x-Rh catalysts

Guishuo Wang, Ran Luo, Chengsheng Yang, Jimin Song, Chuanye Xiong, Hao Tian, Zhi-Jian Zhao, Rentao Mu* & Jinlong Gong*

Key Laboratory for Green Chemical Technology of Ministry of Education, School of Chemical Engineering and Technology, Tianjin University; Collaborative Innovation Center of Chemical Science and Engineering, Tianjin 300072, China

Received May 25, 2019; accepted August 21, 2019; published online October 10, 2019

Metal oxide-promoted Rh-based catalysts have been widely used for CO_2 hydrogenation, especially for the ethanol synthesis. However, this reaction usually suffers low CO_2 conversion and alcohols selectivity due to the formation of byproducts methane and CO. This paper describes an efficient vanadium oxide promoted Rh-based catalysts confined in mesopore MCM-41. The Rh-0.3VO_x/MCM-41 catalyst shows superior conversion (~12%) and ethanol selectivity (~24%) for CO_2 hydrogenation. The promoting effect can be attributed to the synergism of high Rh dispersion by the confinement effect of MCM-41 and the formation of VO_x-Rh interface sites. Experimental and theoretical results indicate the formation of til-CO at VO_x-Rh interface sites is easily dissociated into *CH_x, and then *CH_x can be inserted by CO to form CH_3CO*, followed by CH_3CO* hydrogenation to ethanol.

interfacial active sites, CO_2 hydrogenation, ethanol, Rh-based catalysts, confined catalysts

Citation: Wang G, Luo R, Yang C, Song J, Xiong C, Tian H, Zhao ZJ, Mu R, Gong J. Active sites in CO_2 hydrogenation over confined VO_x-Rh catalysts. *Sci China Chem*, 2019, 62, https://doi.org/10.1007/s11426-019-9590-6

1 Introduction

Carbon dioxide (CO_2) is one of the major emitted greenhouse gases, which can result in climate change and ocean acidification. As a nontoxic, renewable and abundant carbon source, the chemical conversion of CO_2 to value-added chemicals and fuels (oxygenates, alcohols, and olefins etc.) has attracted extensive attention [1–3]. Among these products, higher alcohols ($C_{2+}OH$, especially C_2H_5OH) are preferable from viewpoint of safe transport, higher- energy-densities and good blending flexibility [4]. However, nowadays the production of ethanol mostly relies on the fermentation of cellulosic feedstock [5,6]. The transformation of CO_2 into ethanol remains grand challenge. Because CO_2 is thermodynamically stable and chemically inert molecule, but effectively C=O dissociation and chain growth are needed to produce ethanol.

Therefore, a multifunctional catalyst that can provide active sites for CO dissociative adsorption, CO non-dissociative adsorption and C–C bond formation is needed for CO_2 hydrogenation to ethanol [1,4]. Previous studies have shown that $CoAlO_x$ catalysts with coexisting Co-CoO phases [7] and Pt/Co_3O_4 catalyst using the synergistic effect of water and metallic cobalt [8] achieved 92.1% selectivity of ethanol and 27.3% selectivity of $C_{2+}OH$, respectively. Composite oxide catalyst system has also been used for alcohols synthesis, such as physically mixed Fe-based and Cu-based catalysts [9] and K/Cu-Zn-Fe catalysts [10–12]. Particularly, Rh-based catalysts have been evaluated as promising catalyst system for the selective synthesis of ethanol, due to their special CO dissociation ability [13–16]. Since the main products are CH_4 or CO over pure Rh catalyst [17], a variety of promoters were studied, such as Co, Fe and Li [13,15,16,18]. In addition, high density hydroxyl groups on

*Corresponding authors (email: murt@tju.edu.cn; jlgong@tju.edu.cn)

RhFeLi/TiO_2 nanorods can stabilize formate and protonate methanol, which is easily dissociated to CH_x then is inserted to CH_3CO and hydrogenated to ethanol [19].

Generally, the CO_2 hydrogenation to ethanol reaction pathway contains reverse water gas shift (RWGS), CO dissociation, CO insertion and hydrogenation [15,16,19]. The promoting effect of metal oxide over Rh-based catalysts for CO_2/CO hydrogenation to ethanol was extensively investigated. Several studies have suggested that FeO_x can promote RWGS to activate CO_2 [19], Fe^0 promote CO dissociation and hydrogenation [15] and RhFe alloy was correlated with ethanol selectivity [20,21] in CO_2/CO hydrogenation. MnO_x can also promote CO dissociation by formation of tilted CO species at Rh-MnO interface [22,23]. Generally, the effect of promoter can be ascribed to the electronic interaction [14,16,24,25] and the formation of interfacially active sites between Rh and metal oxide [22,23,26,27].

Since the size effect of Rh nanoparticle can often influence the CO_2 conversion and product selectivity [28,29], MCM-41 was used as support to control the Rh nanoparticle size. Firstly, the influence of various promoters was studied. A significant improvement of CO_2 conversion and ethanol selectivity was observed when vanadium oxide (VO_x) was added to Rh/MCM-41. Furthermore, the VO_x promoting effect on the electronic state of Rh and the reaction mechanism of ethanol formation was investigated.

2 Experimental

2.1 Preparation of catalysts

The catalysts were prepared by the incipient wetness impregnation method. $RhCl_3$•nH_2O (99.9%, Huaweiruike Chemical Co., China), NH_4VO_3 (99.0%, Tianjin Guangfu Technology Development Co. Ltd., China), oxalic acid (99.0%, Aladdin Industrial Corp., China) were used as precursors. MCM-41 (99.9%, NanJingJiCang Nanotechnology Corp., China) with channels diameter between 1.7 to 3.8 nm were used as the support. MCM-41 (1 g) were impregnated with an aqueous solution of oxalic acid (2 mL) containing the precursor [NH_4VO_3/oxalic acid=0.5 (mole ratio)] by using ultrasonication for 1 h. Subsequently, the sample is dried at room temperature overnight and then at 80 °C for 10 h. Finally, the sample is calcined in air at 500 °C for 4 h and reduced in pure H_2 at 400 °C for 1 h. The loading of Rh was controlled at 2 wt%. The loading of VO_x was based on the molar ratio between V and Rh. We named the catalyst as Rh-(y)VO_x/MCM-41, where the y in the bracket repesents the weight percent of V. We prepared Rh-MO_x/MCM-41 (MO_x=WO_x, FeO_x, MnO_x, CeO_x and NbO_x) catalysts by applying the co-impregnation method. We used ammonium metatungstate hydrate (98%, Adamas Reagent Co. Ltd., Germany), $Fe(NO_3)_3$•$9H_2O$ (98%, Alfa Aesar Chemical Co. Ltd., China), 50% Manganous nitrate water solution (99.0%, Tianjin kemi'ou Technology Development Co. Ltd., China), cerium nitrate hexahydrate (98%, Aladdin Chemical Co. Ltd., China) and ammonium niobate(V) oxalate (98%, Alfa Aesar Chemical Co. Ltd., China) as precursors. Then MCM-41 supports (1 g) were impregnated with 2 mL solution of the precursor by using ultrasonication for 1 h. Subsequently, the sample is dried at 80 °C for 10 h, calcined at 500 °C for 4 h and reduced in pure H_2 at 400 °C for 1 h.

2.2 Characterization

X-ray photoelectron spectroscopy (XPS) measurements were taken on a PHI 1600 ESCA instrument (PE Company) which is equipped with an Al Kα X-ray radiation source ($h\nu$= 1,486.6 eV). Before measurements, all the samples were dried at 80 °C for 12 h. The binding energies were calibrated using the C 1s peak at 284.6 eV as a reference. Raman spectra were recorded under ambient conditions using a Renishaw inVia reflex Raman spectrometer with a 325 nm Ar ion laser beam and a 633 nm He-Ne ion laser beam. Before each measurement, the samples were dried at 80 °C for 12 h. The morphology of catalysts was characterized by transmission electron microscopy (TEM; FEI Tecnai G 2 F20, 200 kV, USA) and field emission scanning electron microscopy (FE-SEM; Hitachi S-4800, 5 kV, Japan). The average particle diameter was obtained, after counted over 300 particles. Before each measurement, the samples were dissolved in ethanol and dispersed by using ultrasonication. Powder X-ray diffraction (XRD) patterns were performed with 2θ values between 1° and 60° using a Bruker-D8 diffractormeter (λ=1.54056 Å, Germany). In order to measure the weight content of element Rh and V, 5 mg of each catalyst dissolved in a perchloric/nitric acid mixture, was measured by the inductively coupled plasma optical emission spectroscopy (ICP-OES; Varian 720-ES, USA).

H_2 temperature-programmed reduction (H_2-TPR) and CO_2 temperature-programmed desorption (CO_2-TPD) were performed on a Micromeritics AutoChem II 2920 apparatus equipped with HIDEN QIC-20 mass spectrometer (MS). For H_2-TPR experiment, 100 mg sample was pretreated at 300 °C for 1 h under flowing Ar to remove water and other contamination. After cooling to 50 °C, 10 vol% H_2/Ar was introduced and the temperature was increased from 50 to 800 °C with the ramp rate of 10 °C/min. The signal was recorded online by thermal conductivity detector (TCD). For CO_2-TPD experiment, 100 mg sample was pre-reduced at 400 °C for 1 h under 10 vol% H_2/Ar. When the temperature was cooled and kept stable at 50 °C, pure CO_2 was introduced for 0.5 h. Subsequently, the purging was carried out by Ar for 1 h. Then the temperature was increased from 50 to 600 °C with the ramp rate of 10 °C/min. The gas component

in the effluent was monitored and recorded online by MS, and the signals for *m/z* of 44, 28 and 18 were monitored. The volume of adsorbed CO and metal surface area was studied by employing the CO chemisorption method. For each test, 200 mg sample was pre-reduced with 10 vol% H_2/Ar at 400 °C for 1 h, then cooled to 50 °C. Subsequently, CO was admitted to the sample by injection pulses of 10 vol% CO/He (0.5082 mL) until the consumption peaks became stable. It can be assumed that the adsorption stoichiometry factor of Rh/CO=1.

A Micromeritics Tristar 3000 analyzer (USA) was used to obtain the textual properties of catalysts by N_2 adsorption-desorption at 77 K. Prior to the tests, all samples were degassed at 300 °C for 6 h. The specific surface areas were calculated from the isotherms using the Brunauer-Emmett-Teller (BET) method, and the pore distribution and the cumulative volumes of pores (V_{pore}) were obtained by the Barret-Joyner-Halenda (BJH) method from the desorption branches of the N_2 isotherms.

The diffuse reflectance infrared fourier transform spectroscopy (DRIFTS) was used to record vibrational spectra of molecules adsorbed on the different catalysts. *In situ* DRIFTS experiments were performed on a Thermo Scientific Nicolet IS50 spectrometer (USA), equipped with a Harrick Scientific DRIFTS cell and a mercury-cadmium-telluride (MCT) detector cooled by liquid N_2. To conduct DRIFTS measurement, about 100 mg finely ground sample was packed in the ceramic crucible of the *in-situ* chamber. All the samples were pretreated at 400 °C under a H_2 flow (20 mL/min) for 1 h and cooled to 250 °C in Ar to obtain a background spectrum. The spectra for each measurement were collected by subtracting the background spectrum. Then CO_2/H_2/Ar (CO_2/H_2/Ar=3:1:1, 60 mL/min) mixture gas was introduced. The spectra under reaction conditions were recorded after 64 scans with a resolution of 4 cm^{-1}. As for DRIFTS characterization of CO adsorption, prior to CO-adsorption the samples were pretreated at 400 °C under a H_2 flow (20 mL/min) for 1 h and cooled to the desired temperature to obtain a background spectrum, and the spectra for each measurement was then collected by subtracting the background spectrum. Then CO was flowed into the cell, and the sample surface was saturated. After excess CO was evacuated and the adsorption spectrum was stabilized, CO adsorption spectra at desired temperature were collected. For *in situ* CO-DRIFTS experiments, the samples were reduced at 400 °C for 1 h in H_2 (30 mL/min) with a ramping rate of 4 °C/min. Before CO adsorption, Ar (30 mL/min) was switched to purge the residual H_2. The background spectra were collected after cooling down to room temperature. Spectra were collected with temperature rising from 30 to 50, 100, 150, 200 and 250 °C and hold 30 min.

Spin polarized periodic density functional theory (DFT) calculations were carried out to model VO_x-Rh catalyst from theory perspective using Vienna *ab initio* simulation package [30,31]. We employed Perdew-Burke-Ernzerh (PBE) of exchange-correlation functional [32]. The valence wave functions were expanded by plane wave with a cutoff energy of 400 eV, while atomic core was described by the Projected Augmented Wave (PAW) pseudopotentials [33]. A Monkhorst-Pack *k*-point sampling was applied with a 3×3×1 *k*-points grid which was tested to the convergence with the criterion of H atom adsorption energy variation smaller than 0.1 eV. The (4×4) surface model was created by cutting the Rh unit cell of the bulk phase along the (111) plane and VO_x species with different degrees of polymerization were added on Rh surface. The thickness of the employed slabs is four layers, with top two layers relaxed on each surface. During the geometry optimization, the whole slab together with the adsorbate was relaxed. A vacuum layer of 15 Å was implemented in order to avoid the interactions between slabs.

The adsorption energies were calculated based on the following equation:

$$\Delta E_{ads} = E_{adsorbate+surface} - E_{surface} - E_{gas}$$

where $E_{adsorbate+surface}$ refers to the total energy of slab with adsorbates while $E_{surface}$ denotes as the clean slab. We utilize gas phase total energy of adsorbates as reference, which is defined as E_{gas}. When modeling the gas phase molecule, we adapted the cubic unit cell with sides length of 15 Å. All the structures were optimized until the force on each atom was less than 0.02 eV/Å.

The formation energies of oxygen vacancy were calculated based on the following equation:

$$\Delta E_V = E_{surface\ with\ O_v} + E_{H_2O(g)} - E_{perfect\ surface} - E_{H_2(g)}$$

We use energy of gas phase H_2O and H_2 as reference to match the reduction process in experiment.

The transition states were located by climbing-image nudged elastic band method [34]. The activation barrier was defined as the difference in energy between the preceding lowest energy intermediate E_{IS} and the transition state E_{TS}:

$$E = E_{TS} - E_{IS}$$

2.3 Catalyst test

To examine the catalytic performance of catalysts, 300 mg of each catalyst with a 20–40 mesh size distribution was mixed with 2.0 g of quartz particles (SiC: granulation of 0.075–0.4 mm) to avoid hot spots and pressure drop across bed and packed in the stainless steel (8 mm×400 mm) tubular reactor. Prior to each experiment, the catalyst was activated by reducing in H_2 atmosphere (99.99%) with the flow rate of 30 mL/min and the temperature of 400 °C for 1 h. After the reduction of catalyst, the reactor was cooled down to reaction temperature. Then the reactant gases (CO_2 and H_2 with molar ratio of 1:3, 3.0 MPa) were introduced into the reactor. The

gas hourly space velocity (GHSV) was set at 6,000 h^{-1}. The product gas was analyzed with an online gas chromatograph (GC, Agilent 7890B, USA) equipped with two detectors. One is flame ionization detector (FID) with a HP-FFAP column using H_2 as a carrier gas to analyze the organic species such as alcohols, oxygenate and hydrocarbons. The other one is TCD with columns of MS-5A column and Hayesep Q using He as a carrier gas to monitor the incondensable gas species including H_2, CO_2, N_2, CO and CH_4. All the flow lines between the reactor and the GC were heated and kept beyond 150 °C, to avoid the liquefaction of the alcohols products. CO_2 conversion, C-containing gas products selectivity, ethanol yield and turnover frequency (TOF) were calculated as follow [12]:

$$X_{CO_2}(\%) = \frac{F_{CO_2,in} - F_{CO_2,out}}{F_{CO_2,in}} \times 100$$

$$S_i(\%) = \frac{\%i \times n}{\sum((\%i) \times n)} \times 100$$

$$STY_{ROH} = \frac{F_{CO_2,in} \times X_{CO_2} \times 60 \times S_{ROH} \times M_{ROH}}{22.4 \times m_{cat.}} \ (g/(kg_{cat.}\ h))$$

$$TOF_{ROH} = \frac{STY_{ROH} \times 0.3 \times 22.4}{V_{CO} \times SF \times M_{ROH}} \ (h^{-1})$$

where i represents the carbon containing species in the products, including CH_4, CO, C_nH_m, CH_3OH and C_2H_5OH, and n is the number of carbon atoms in the carbon containing species, V_{CO} is the volume of adsorbed CO (mL), SF is the stoichiometry factor. TOF of ethanol was calculated as moles of ethanol formed on per mole of surface Rh obtained from the CO chemisorption. The data for the catalytic activity were collected when the reaction reached stable after 15 h, and the repeated tests have been also carried out to confirm the reproducibility of the results. Besides, carbon balances closed to within ±5% for the data.

3 Results and discussion

3.1 Catalyst structure

The morphology of Rh/MCM-41catalysts and Rh-0.3VO_x/MCM-41catalysts are shown in Figure 1(a, b), respectively. The Rh nanoparticles (NPs) confined in MCM-41channels present uniform size distribution with an average diameter of 2.1±1.0 nm (Figure 1(a, b)). As shown in Figure 1(b), the addition of VO_x does not change the size distribution of the Rh NPs due to the confinement effect of MCM-41. The specific surface area of Rh-VO_x/MCM-41 is determined to be 348–389 m^2/g_{cat}, which is close to the half of the MCM-41 (793 m^2/g_{cat}) (Table S1, Supporting Information online). The pore volume of Rh-VO_x/MCM-41 is determined to be 0.294–0.322 cm^3/g_{cat}, which is also close to the half of the MCM-41 (0.707 cm^3/g_{cat}). However, SEM images show that there is no severe aggregation of MCM-41 after the impregnation (Figure S1(a, b), Supporting Information online). In addition, the meso-structures of MCM-41 remain unchanged after the impregnation (Figure S2). These results indicate that part of MCM-41channels should be filled by Rh-VO_x nanoparticles.

To verify the surface configuration of VO_x species on the MCM-41, Raman studies with 325 and 633 nm excitation wavelength were employed. Specifically, UV Raman is more sensitive in monitoring the isolated and polymerized VO_x species [35,36]. While Raman spectroscopy with excitation wavelength 633 nm was applied to observe RhO_x stretch feature [37]. As shown in Figure 1(c), the broad band at 487 cm^{-1} in the spectra is assigned to the D1 defect mode of silica support [38]. There is a sharp band at 1,021–1,025 cm^{-1} assigned to V=O band when the loading of VO_x is higher than 0.3 wt% in Rh-(y)VO_x/MCM-41. When the loading of VO_x is higher than 0.5 wt%, a new band assigned to crystalline V_2O_5 at 993 cm^{-1} appears and the peak intensity rises with the loading of VO_x is further increasing [36,38]. As shown in Figure 1(d), the Raman bands of Rh_2O_3 (265, 470, 560 cm^{-1}) in Rh/MCM-41 are consistent with those observed previously [37]. The bands in VO_x/MCM-41 at 250, 305, 450 cm^{-1} can be attributed to VO_x. However, the spectrum of Rh-VO_x/MCM-41 significantly differs from the linear combination of that from Rh/MCM-41 and VO_x/MCM-41. Clearly, the addition of V altered the bonding of Rh–O and V–O due to the strong interaction between Rh and VO_x [39,40].

H_2-TPR studies of Rh-(y)VO_x/MCM-41were carried out to investigate the strong interaction between Rh and oxide promoters (Figure 1(e)). The peaks centered below 200 °C can be ascribed to the reduction of Rh_2O_3 [15]. When the VO_x was added, the Rh_2O_3 reduction peak becomes broader and moved to higher temperature, indicating VO_x may hinder the reduction of Rh_2O_3 [27,41]. It is noteworthy that there is no reduction peak at 300–500 °C can be observed, which is assigned to bulk V_2O_5 reduction.

To further quantitative study the exposed active Rh sites of Rh-(y)VO_x/MCM-41 catalysts, CO titration experiments were conducted. The adsorbed amount of CO for Rh/MCM-41 is determined to be 20 μmol/g. As the loading of VO_x increases from 0.1 wt% to 1.0 wt%, the adsorbed amount of CO decreases from 16 to 9 μmol/g (Table S1). Since the size of Rh-based catalysts does not change over different samples, the observed low adsorption amount of CO on Rh-(y)VO_x/MCM-41 can be attributed to the partial encapsulation of Rh sites by VO_x overlayers [39,40]. Raman spectroscopy also demonstrates the strong interaction between Rh and VO_x (Figure 1(c, d)). Consequently, a catalyst structure of Rh nanoparticles partially covered by VO_x was proposed.

XPS analysis was also conducted to investigate the surface structure of Rh-based catalysts. As shown in Figure 1(f),

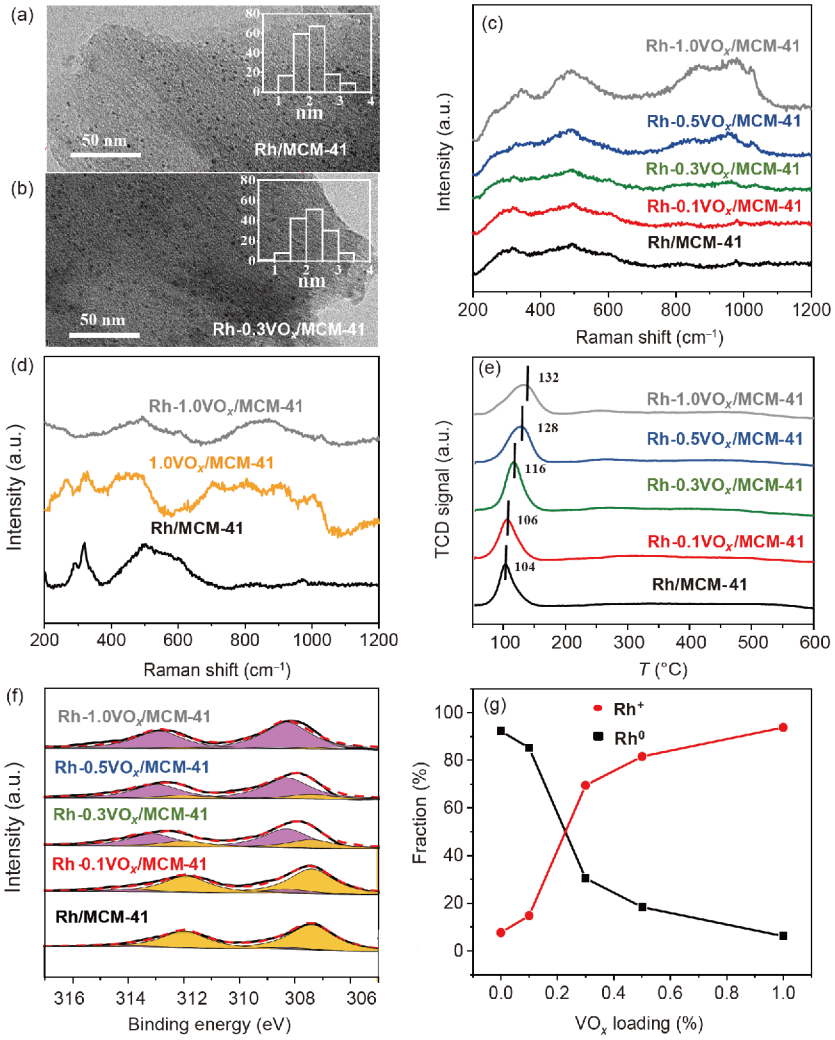

Figure 1 TEM images of (a) Rh/MCM-41 and (b) Rh-0.3VO_x/MCM-41 catalysts after CO_2 hydrogenation reaction at 250 °C, 3 MPa for 12 h. Insets indicate the size distribution of the Rh-based catalysts. (c) UV ($\lambda_{excitation}$=325 nm) Raman spectra of the Rh-(y)VO_x/MCM-41catalysts, and (d) $\lambda_{excitation}$= 633 nm Raman spectra of Rh-1.0VO_x/MCM-41, 1.0VO_x/MCM-41 and Rh/MCM-41. (e) H_2-TPR profiles of the Rh-(y)VO_x/MCM-41 catalysts. (f) XPS Rh 3d peak for Rh/MCM-41, Rh-0.1VO_x/MCM-41, Rh-0.3VO_x/MCM-41, Rh-0.5VO_x/MCM-41, Rh-1.0VO_x/MCM-41 after CO_2 hydrogenation reaction at 250 °C, 3 MPa for 12 h. (g) The relative fraction of Rh^+ and Rh^0 as a function of VO_x loading in Rh-(y)VO_x/MCM-41 catalysts (color online).

deconvolution of the Rh $3d_{5/2}$ peak for Rh-(y)VO_x/MCM-41 catalysts yields two peaks centered at 307.4 and 308.3 eV, corresponding to metallic Rh^0 and oxidic Rh^+ species, respectively [23,25,42]. Furthermore, the relative percentage of Rh^0 and Rh^+ was estimated and shown in Figure 1(g). With the loading of VO_x increasing, Rh^+/Rh^0 ratio increased significantly. This is consistent with H_2-TPR and Raman results. The XPS spectra of V $2p_{3/2}$ signal and fitting curve of the Rh-0.5VO_x/MCM-41 and Rh-1.0VO_x/MCM-41 catalysts were also shown in Figure S3. When the loading of VO_x is 0.5 wt%, the fraction of V^{5+}, V^{4+} and V^{3+} is 0%, 60.5% and 39.5%, respectively. However, the fraction of V^{5+}, V^{4+} and V^{3+} is determined to 45.8%, 36.6% and 17.6%, respectively, as the loading of VO_x is increased to 1.0 wt%. We also studied the VO_x/Rh catalysts with different VO_x loadings from theory perspective. In order to match the tendency that the degree of polymerization of VO_x increases with VO_x loading, we induced the monomer (V1), dimer (V2), trimer (V3) and tetramer (V4) vanadium oxide species on the Rh(111) surface (Figure S4). In these models we found that the Bader Charge value of VO_x cluster changes from $-0.82e^-$ to $-0.1e^-$ after added on Rh(111), which means that the Rh(111) base provides electrons to the VO_x (Figure S5). These observations clearly demonstrate the interfacially electronic interaction between VO_x and Rh.

3.2 Catalyst performance

Firstly, the catalytic performance of Rh/MCM-41 catalysts with different promoters which are often used in CO_2/CO hydrogenation is studied (Figures 2(a), S6 and Table S2) [6,24,43]. The VO_x promoted catalyst shows the highest ethanol selectivity and yield. Subsequently, the catalytic performance to CO_2 hydrogenation is studied over Rh/

MCM-41 with different loadings of VO_x (Figure 2(b)). The detailed values of CO_2 conversion and the selectivity to different products are presented in Table 1, and the carbon balance is between 0.95 to 0.98. Unpromoted Rh/MCM-41 presents CO_2 conversion and ethanol selectivity of 2.3% and 4.4%. We find that CO_2 conversion and ethanol selectivity is increased to 8.9% and 15.4% after 0.1 wt% VO_x is added. When the loading of VO_x is 0.3 wt%, the CO_2 conversion and the selectivity to ethanol reach the highest value of 12% and 24%, respectively. However, CO_2 conversion and the selectivity of ethanol decrease when the loading of VO_x is further increased. The decrease of CO_2 conversion indicates that excess VO_x has a passive effect, which may be caused by the excessive encapsulation of Rh sites by VO_x species. This suggestion has been proven by Raman spectroscopy combined with CO chemisorption (Table S1, Figure 1(c, d)). In addition, as the loading of VO_x increases, the selectivity of CH_4 increases and the selectivity of CO decreases. The CH_4 and CH_3– in ethanol comes from the dissociation of CO, while CO, methanol and –CH_2OH come from the non-dissociation of CO [24]. As thus, a descriptor (C_{dis}/C_{ins}) is defined to evaluate the presence of two carbon-containing species in the reaction products related to CO dissociation (C_{dis}) and non-dissociative CO insertion (C_{ins}), respectively. As shown in Table 1, the C_{dis}/C_{ins} increases with the loading of VO_x increasing. Based on these results, we conclude that the addition of VO_x can increase the yield of ethanol by promoting the CO_2 activation and CO dissociation, while excess VO_x suppresses CO_2 conversion by blocking Rh sites.

We also study the effects of different reaction conditions, including temperature, pressure and space velocity on the activity and selectivity of Rh-0.3VO_x/MCM-41 (Figure S7). It can be seen that the moderate temperature, low weight space velocity and high pressure reaction condition preferentially produce ethanol, which is consistent with thermodynamic analysis [44,45].

3.3 Promotion effects of the VO_x

The CO adsorption properties on promoted and unpromoted Rh catalysts are investigated using DRIFTS at 50 and 250 °C. As shown in Figure 3(a), the major adsorption peak at 2,051–2,061 cm^{-1} can be assigned to linear CO (lin-CO) adsorption [15,23,28]. The peaks at ~2,080 and ~2,010 cm^{-1} are associated with the symmetric and asymmetric stretches of $Rh(CO)_2$ gem-dicarbonyl species (gem-CO) adsorbed at Rh^+ sites [26,46]. The peak at lower wavenumber (~1,910 cm^{-1}) corresponds to bridging CO adsorption at two or more Rh atoms [15,26,28,47]. When VO_x is added, the peak position of gem-CO and lin-CO does not shift. However, the intensity of gem-CO is increased, because the fraction of Rh^+ increases with VO_x added. While there is a broader peak from 1,900 to 1,750 cm^{-1} appearing when VO_x is added. This broad peak should contain two kinds of CO adsorbed peaks, the bridged CO and tilted CO [26]. Further, *in situ* CO-DRIFTS is employed to study the evolution of CO

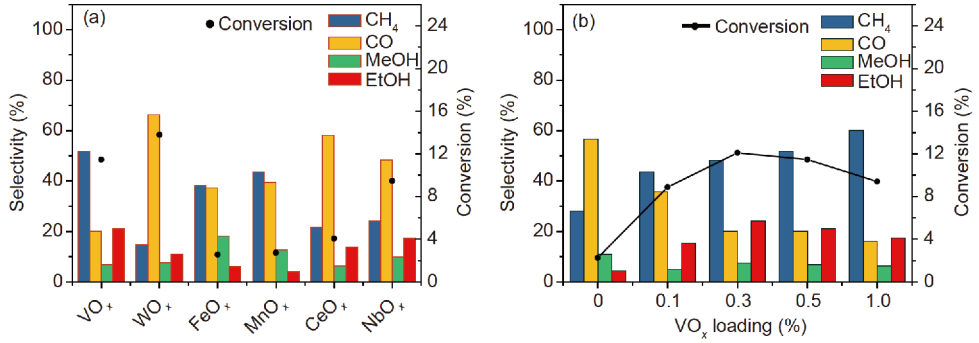

Figure 2 (a) Catalytic performance to CO_2 hydrogenation over Rh/MCM-41catalysts with various promoters. The loading of VO_x is 0.5 wt% and the loadings of other promoters are controlled at their optimized values. (b) Catalytic performance to CO_2 hydrogenation over Rh/MCM-41 catalysts with different VO_x loadings. Reaction conditions: P=3.0 MPa; T=250 °C; weight space velocity is 6,000 h^{-1}; $H_2/CO_2/N_2$=3:1:1 (color online).

Table 1 Catalytic performance of Rh/MCM-41 catalysts with different VO_x loadings [a)]

VO_x loading	Conversion (C%)	Selectivity of products (C%)				STY (EtOH) (g/(kg h))	TOF (EtOH) (h^{-1})	C_{dis}/C_{ins}	Carbon balance
		CH_4	CO	MeOH	EtOH				
0	2.3	28.1	56.6	0.51	4.4	1.7	0.51	0.45	0.97
0.1	8.9	43.7	35.8	8.34	15.4	22.5	8.34	1.04	0.97
0.3	12.1	48.3	20.1	17.75	24.1	47.9	19.30	1.40	0.98
0.5	11.5	51.7	20.2	19.30	21.2	40.1	18.22	1.51	0.96
1.0	9.4	60.0	16.0	18.22	17.5	27.0	17.75	1.94	0.95

a) Reaction conditions: P=3.0 MPa; T=250 °C; weight space velocity is 6,000 h^{-1}; $H_2/CO_2/N_2$=3:1:1.

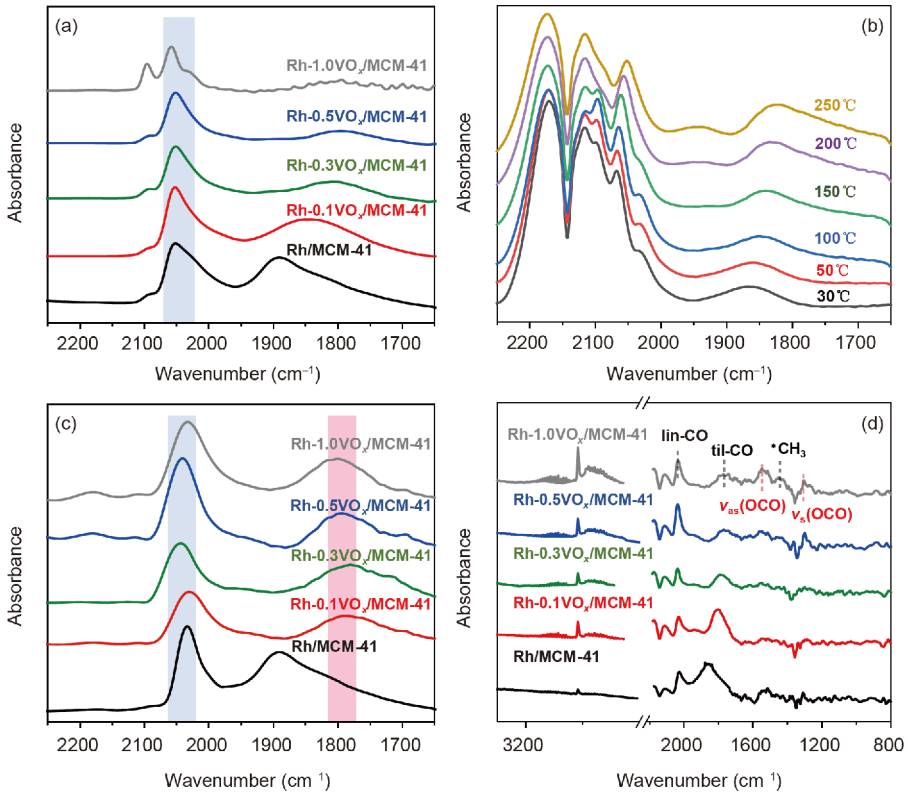

Figure 3 The CO DRIFTS spectra of (a) 50 °C on Rh-(y)VO$_x$/MCM-41catalysts, (b) from 30 to 250 °C on Rh-0.3VO$_x$/MCM-41, (c) 250 °C on Rh-(y)VO$_x$/MCM-41 catalysts. (d) In situ DRIFTS spectra of the Rh-(y)VO$_x$/MCM-41 catalysts in reaction at 250 °C, H_2/CO_2=3:1 (color online).

adsorption with temperature increasing from 30 to 250 °C on Rh-0.3VO$_x$/MCM-41. As shown in Figure 3(b), the broad peak centered at 1,850 cm^{-1} is decomposed to two peaks which centered at 1,920 and 1,810 cm^{-1} when temperature increases from 30 to 250 °C. These two peaks can be ascribed to bridging CO adsorption and tilted CO adsorption, respectively.

As shown in Figure 3(c), the gem-dicarbonyl species disappeared at 250 °C. At this temperature, the most prominent feature is the vibrational frequency at 2,051–2,061 cm^{-1} which can be attributed to linearly adsorbed CO on Rh^0 sites [28,46]. We find that the peak position of linear CO and bridging CO shifts to higher wavenumber when VO$_x$ is added. This observed shift can be ascribed to the deficient electron state of Rh$^+$, caused by interfacially electronic interaction between VO$_x$ and Rh [24]. When VO$_x$ is added, the bridging CO peak centered at ~1,910 cm^{-1} becomes small. While a strong, lower wavenumber peak around 1,780 cm^{-1} is observed. This peak can be assigned to tilted CO at the metal/oxide interface, in which the C atom of CO molecules is bonded to the Rh sites while the O atom interacts with V$^{\delta+}$ cation sites [23,26,48,49].

In-situ DRIFTS was further carried out to investigate the influence of VO$_x$ on the ethanol formation (Figure 3(d)). In the ν_{C-H} region, the bands at 3,016, 2,965, 2,880 and 2,744 cm^{-1} were observed, stemming from gaseous CH$_4$ (3,016 cm^{-1}) and adsorbed formate species, respectively. In the O–C–O stretching region between 1,650 and 1,200 cm^{-1}, the bands at 1,585 and 1,370 cm^{-1} were assigned to adsorbed formate, while the rest peaks might stem from carbonate (Table S3) [50–52]. CO$_2$-TPD studies show that there is only one peak centered at 110 °C for unpromoted Rh/MCM-41 (Figure S8). When the loading of VO$_x$ loading is higher than 0.3 wt%, a peak centered at 220 °C appears. It is suggested that a new CO$_2$ adsorption site was created when VO$_x$ was added, and CO$_2$ adsorption capacity increased. As shown in Figure 3(d), the peaks assigned to formate became stronger with VO$_x$ addition. It is proposed that CO$_2$ hydrogenation followed the path of carbonate and formate from CO$_2$ adsorbed on the surface of Rh-(y)VO$_x$/MCM-41. The formation of ethanol from CO$_2$ hydrogenation could be the result of CO produced by RWGS [53], and CO insertion could be responsible for the chain lengthening [54,55]. Thus, it is proposed that ethanol can be synthesized by CO insertion into *CH$_3$ species to form CH$_3$CO*, followed by CH$_3$CO* hydrogenation [15,16]. In this reaction pathway, it is generally agreed that the CO dissociation is the rate limiting step over Rh [56], and the initial C–C bond formation influences C_{2+}OH productivity significantly [57]. As expected, significant amounts of *CH$_3$ species (1,470 cm^{-1}) are observed on the surface of Rh-(y)VO$_x$/MCM-41 and increased with VO$_x$ added [58,59]. Subsequently, these abundant adsorbed

*CH_3 species on Rh-(y)VO_x/MCM-41 can be inserted by CO, which may be responsible for the high ethanol yield.

We also used the models with different degrees of polymerization of VO_x mentioned before to study the formation of interfacial sites and their CO adsorption and dissociation performance. VO_x clusters were reduced by H_2 in the first place and formed two kinds of oxygen vacancy (Ov1: Ov between V and Rh; Ov2: Ov between two V atoms), corresponding oxygen vacancy formation energy is shown in Figure 4(a). Then CO can adsorb on the interface of Rh and VO_x with O absorbing on Ov and C absorbing on Rh surface (Ov1-Rh site and Ov2-Rh site, Figure S9). As shown in Figure 4(a), the adsorption energies of CO on all the interfacial Ov-Rh sites of VO_x/Rh(111) are higher than that of Rh(111) hcp site from −0.69 to −0.13 eV. We further considered the CO dissociation process on the interfacial Ov-Rh sites, which is found that the activation energies for CO dissociation on these sites are lower than that on pure Rh surface. So as to explain this trendency of activation energy, we found a linear relationship between CO absorbed bond lengths and activation energies of different sites and models. As shown in Figure 4(b), the C–O bond lengths are longer than that of CO adsorption on Rh(111), indicates that CO can be well activated on the interfacial sites. Thus, these VO_x-Rh interfacial sites which can accelerate CO dissociation process may be responsible for the high ethanol yield.

In order to quantify the capacity of CO dissociation, we integrated the peak of lin-CO and til-CO in the DRIFTS spectra of the Rh-(y)VO_x/MCM-41 catalysts at 250 °C (Figure S10). The peak area of lin-CO and til-CO and ratio of til-CO/lin-CO is shown in Table S4. It is interesting that the til-CO/lin-CO is determined to be 0.99 when the loading of VO_x is 0.3 wt%. This is well consistent with the observed highest ethanol yield over Rh-0.3VO_x/MCM-41 catalyst. In addition, we also show that the relative fraction of Rh^+ is increased significantly with the addition of VO_x (Figure 1(g)). These results suggest that the VO_x promoter can induce the formation of Rh^+ species on Rh-(y)VO_x/MCM-41 catalyst, due to the interfacially electronic interaction between Rh and VO_x promoter. The selectivity descriptor of C_{dis}/C_{ins} is plotted in Figure 4(c, d) as a function of the ratio of til-CO/lin-CO and the fraction of VO_x induced Rh^+, respectively. We find that the selectivity of C_{dis}/C_{ins} increases linearly with the ratio of til-CO/lin-CO and the fraction of Rh^+ species. Therefore, it can be concluded that the amount of tilted C–O species can be increased as the number of the VO_x-Rh interfacial sites increasing. Adsorption of tilted C–O species makes the C–O bond breaking easily and hydrogenated to form *CH_3, hence inserted to CH_3CO*, hydrogenated to ethanol, as shown in Scheme 1.

4 Conclusions

In summary, our study provides a quantitative assessment of the correlation between interfacial active sites and catalytic

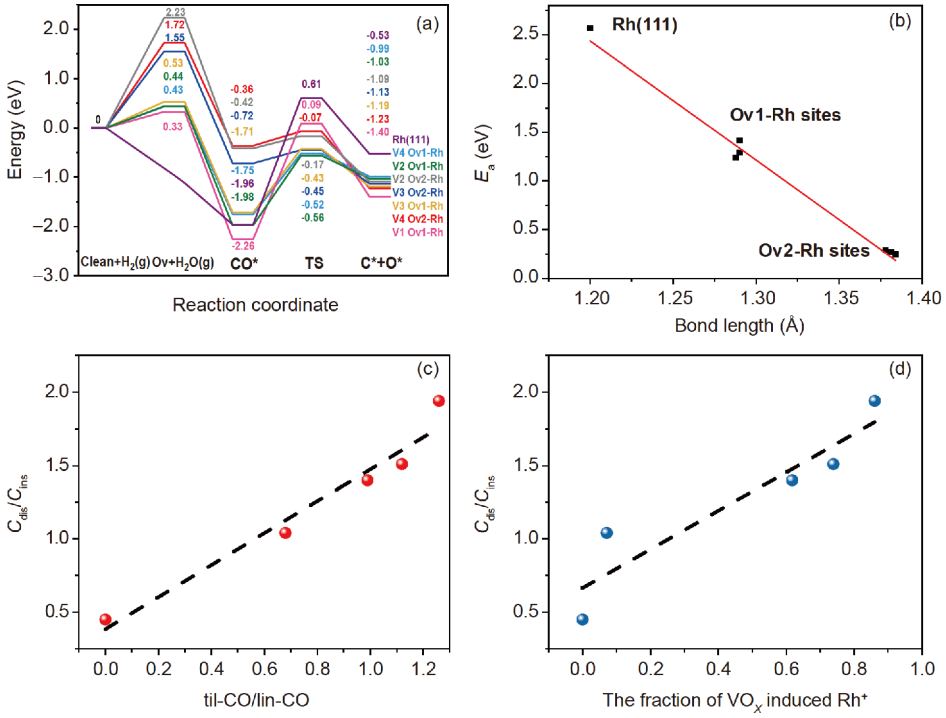

Figure 4 (a) Potential energy diagram for the CO dissociation on VO_x/Rh(111) with VO_x speciecs from monomer to tetramer. (b) The activation energy of CO as a function of CO bond length. Evolution of the selectivity parameter C_{dis}/C_{ins} with (c) the ratio of til-CO/lin-CO and (d) VO_x induced Rh^+ fraction (color online).

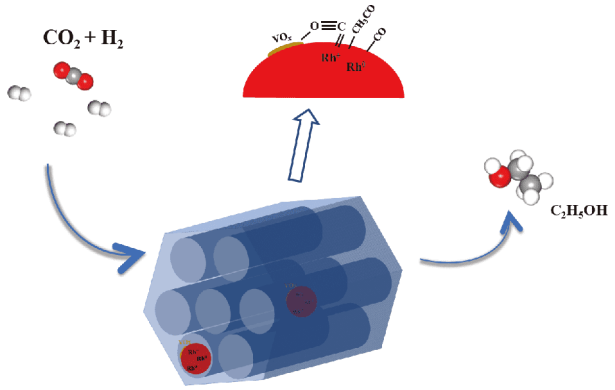

Scheme 1 Schematic of CO_2 hydrogenation over VO_x promoted Rh-based catalyst in MCM-41. The VO_x plays an important role in promoting the dissociation of CO and promoting the formation of ethanol (color online).

performance in CO_2 hydrogenation over multifunctional Rh-VO_x/MCM-41 catalysts, which has never been proposed. We clearly demonstrated that the promotion of VO_x on Rh/MCM-41 can be attributed to the electronic effect that induces the generation of Rh^+ species and the formation of interfacial VO_x-Rh active sites. Based on H_2-TPR, XPS, *in-situ* spectroscopic characterizations and DFT calculations, we propose that the til-CO adsorbed at the interface of VO_x-Rh can be easily dissociated into *CH_x, thus favoring the formation of ethanol upon CO insertion. When the loading of VO_x is 0.3 wt%, the amount of dissociative adsorbed CO is almost equal to that of non-dissociative adsorbed CO, resulting in the highest ethanol selectivity and yield. We also expect that the interfacial catalysis between metal and metal oxide may be widely applied in other catalytic systems.

Acknowledgements This work was supported by the National Key R&D Program of China (2016YFB0600901), the National Natural Science Foundation of China (21525626, 21603159, 21676181), and the Program of Introducing Talents of Discipline to Universities (B06006).

Conflict of interest The authors declare that they have no conflict of interest.

Supporting information The supporting information is available online at http://chem.scichina.com and http://link.springer.com/journal/11426. The supporting materials are published as submitted, without typesetting or editing. The responsibility for scientific accuracy and content remains entirely with the authors.

1 Wang W, Wang S, Ma X, Gong J. *Chem Soc Rev*, 2011, 40: 3703
2 Porosoff MD, Yan B, Chen JG. *Energy Environ Sci*, 2016, 9: 62–73
3 Yang H, Zhang C, Gao P, Wang H, Li X, Zhong L, Wei W, Sun Y. *Catal Sci Technol*, 2017, 7: 4580–4598
4 Aresta M, Dibenedetto A, Angelini A. *Chem Rev*, 2014, 114: 1709–1742
5 Devarapalli M, Atiyeh HK. *Biofuel Res J*, 2015, 2: 268–280
6 Luk HT, Mondelli C, Ferré DC, Stewart JA, Pérez-Ramírez J. *Chem Soc Rev*, 2017, 46: 1358–1426
7 Wang L, Wang L, Zhang J, Liu X, Wang H, Zhang W, Yang Q, Ma J, Dong X, Yoo SJ, Kim JG, Meng X, Xiao FS. *Angew Chem Int Ed*, 2018, 57: 6104–6108
8 He Z, Qian Q, Ma J, Meng Q, Zhou H, Song J, Liu Z, Han B. *Angew Chem Int Ed*, 2016, 55: 737–741
9 Inui T, Yamamoto T, Inoue M, Hara H, Takeguchi T, Kim JB. *Appl Catal A-Gen*, 1999, 186: 395–406
10 Takagawa M, Okamoto A, Fujimura H, Izawa Y, Arakawa H. *Stud Surf Sci Catal*, 1998, 114: 525–528
11 Higuchi K, Haneda Y, Tabata K, Nakahara Y, Takagawa M. *Stud Surf Sci Catal*, 1998, 114: 517–520
12 Li S, Guo H, Luo C, Zhang H, Xiong L, Chen X, Ma L. *Catal Lett*, 2013, 143: 345–355
13 Kusama H, Okabe K, Sayama K, Arakawa H. *Appl Organometal Chem*, 2000, 14: 836–840
14 Kitamura Bando K, Soga K, Kunimori K, Arakawa H. *Appl Catal A-Gen*, 1998, 175: 67–81
15 Kusama H, Okabe K, Sayama K, Arakawa H. *Energy*, 1997, 22: 343–348
16 Kusama H, Okabe K, Sayama K, Arakawa H. *Catal Today*, 1996, 28: 261–266
17 Kusama H, Bando KK, Okabe K, Arakawa H. *Appl Catal A-Gen*, 2001, 205: 285–294
18 Kusama H, Okabe K, Arakawa H. *Appl Catal A-Gen*, 2001, 207: 85–94
19 Yang C, Mu R, Wang G, Song J, Tian H, Zhao ZJ, Gong J. *Chem Sci*, 2019, 10: 3161–3167
20 Carrillo P, Shi R, Teeluck K, Senanayake SD, White MG. *ACS Catal*, 2018, 8: 7279–7286
21 Palomino RM, Magee JW, Llorca J, Senanayake SD, White MG. *J Catal*, 2015, 329: 87–94
22 Wang Y, Luo H, Liang D, Bao X. *J Catal*, 2000, 196: 46–55
23 Yang N, Yoo JS, Schumann J, Bothra P, Singh JA, Valle E, Abild-Pedersen F, Nørskov JK, Bent SF. *ACS Catal*, 2017, 7: 5746–5757
24 Prieto G, Concepción P, Martínez A, Mendoza E. *J Catal*, 2011, 280: 274–288
25 Chen Y, Zhang H, Ma H, Qian W, Jin F, Ying W. *Catal Lett*, 2018, 148: 691–698
26 Schwartz V, Campos A, Egbebi A, Spivey JJ, Overbury SH. *ACS Catal*, 2011, 1: 1298–1306
27 Mo X, Gao J, Umnajkaseam N, Goodwin Jr. JG. *J Catal*, 2009, 267: 167–176
28 Matsubu JC, Yang VN, Christopher P. *J Am Chem Soc*, 2015, 137: 3076–3084
29 Arakawa H, Takeuchi K, Matsuzaki T, Sugi Y. *Chem Lett*, 1984, 13: 1607–1610
30 Kresse G, Hafner J. *Phys Rev B*, 1993, 47: 558–561
31 Kresse G, Furthmüller J. *Phys Rev B*, 1996, 54: 11169–11186
32 Perdew JP, Burke K, Ernzerhof M. *Phys Rev Lett*, 1996, 77: 3865–3868
33 Blöchl PE. *Phys Rev B*, 1994, 50: 17953–17979
34 Henkelman G, Uberuaga BP, Jónsson H. *J Chem Phys*, 2000, 113: 9901–9904
35 Wu Z, Kim HS, Stair PC, Rugmini S, Jackson SD. *J Phys Chem B*, 2005, 109: 2793–2800
36 Liu G, Zhao ZJ, Wu T, Zeng L, Gong J. *ACS Catal*, 2016, 6: 5207–5214
37 Pan X, Fan Z, Chen W, Ding Y, Luo H, Bao X. *Nat Mater*, 2007, 6: 507–511
38 Bulánek R, Čičmanec P, Setnička M. *Phys Procedia*, 2013, 44: 195–205
39 Kip BJ, Smeets PAT, van Grondelle J, Prins R. *Appl Catal*, 1987, 33: 181–208
40 Beutel T, Siborov V, Tesche B, Knözinger H. *J Catal*, 1997, 167: 379–390
41 Yamagishi T, Furikado I, Ito S, Miyao T, Naito S, Tomishige K, Kunimori K. *J Mol Catal A-Chem*, 2006, 244: 201–212
42 Liu Y, Göeltl F, Ro I, Ball MR, Sener C, Aragão IB, Zanchet D, Huber GW, Mavrikakis M, Dumesic JA. *ACS Catal*, 2017, 7: 4550–4563

43 Zhang W, Wang L, Liu H, Hao Y, Li H, Khan MU, Zeng J. *Nano Lett*, 2017, 17: 788–793
44 Swapnesh A, Srivastava VC, Mall ID. *Chem Eng Technol*, 2014, 37: 1765–1777
45 He X. *Int J Oil Gas Coal Eng*, 2017, 5: 145–152
46 Heyl D, Rodemerck U, Bentrup U. *ACS Catal*, 2016, 6: 6275–6284
47 Matsubu JC, Zhang S, DeRita L, Marinkovic NS, Chen JG, Graham GW, Pan X, Christopher P. *Nat Chem*, 2017, 9: 120–127
48 Stevenson SA, Lisitsyn A, Knoezinger H. *J Phys Chem*, 1990, 94: 1576–1581
49 Wang Y, Song Z, Ma D, Luo H, Liang D, Bao X. *J Mol Catal A-Chem*, 1999, 149: 51–61
50 Wang J, Li G, Li Z, Tang C, Feng Z, An H, Liu H, Liu T, Li C. *Sci Adv*, 2017, 3: e1701290
51 Graciani J, Mudiyanselage K, Xu F, Baber AE, Evans J, Senanayake SD, Stacchiola DJ, Liu P, Hrbek J, Fernández Sanz J, Rodriguez JA. *Science*, 2014, 345: 546–550
52 Wang X, Hong Y, Shi H, Szanyi J. *J Catal*, 2016, 343: 185–195
53 Chen Y, Choi S, Thompson LT. *J Catal*, 2016, 343: 147–156
54 Schweicher J, Bundhoo A, Kruse N. *J Am Chem Soc*, 2012, 134: 16135–16138
55 Zhao YH, Sun K, Ma X, Liu J, Sun D, Su HY, Li WX. *Angew Chem Int Ed*, 2011, 50: 5335–5338
56 Kusama H, Bando KK, Okabe K, Arakawa H. *Appl Catal A-Gen*, 2000, 197: 255–268
57 Sun J, Cai Q, Wan Y, Wan S, Wang L, Lin J, Mei D, Wang Y. *ACS Catal*, 2016, 6: 5771–5785
58 Kattel S, Yu W, Yang X, Yan B, Huang Y, Wan W, Liu P, Chen JG. *Angew Chem Int Ed*, 2016, 55: 7968–7973
59 Kattel S, Liu P, Chen JG. *J Am Chem Soc*, 2017, 139: 9739–9754